

Applying the Techniques of Microstructural Image Processing Towards Measuring Interface Angles in Unsaturated Geomaterials

Mohammad Motalleb Nejad, S.M.ASCE,¹ Kalehiwot Nega Manahiloh, M.ASCE,² and Christopher L. Meehan, M.ASCE³

¹Graduate Student, Dept. of Civil and Environmental Engineering, University of Delaware, 301 DuPont Hall, Newark, DE 19716, U.S.A.; e-mail: mohmtlb@udel.edu

²Assistant Professor, Dept. of Civil and Environmental Engineering, University of Delaware, 301 DuPont Hall, Newark, DE 19716, U.S.A.; e-mail: knega@udel.edu

³Bentley Systems Incorporated Chair of Civil Engineering & Associate Professor, Dept. of Civil and Environmental Engineering, University of Delaware, 301 DuPont Hall, Newark, DE 19716, U.S.A.; e-mail: cmeehan@udel.edu

ABSTRACT

Previously, researchers have examined phase interactions in multi-phase systems such as geomaterials at different degrees of saturation. Some studies have measured the angle made by the solid-liquid and liquid-air interfaces using physical laboratory tests. The lack of technological advancements that enabled microstructural inter-phase examination has largely impeded results from such efforts. In addition, the measurement of contact angle has largely been dominated by user interference. Recent developments in image acquisition and associated advanced image processing platforms have enabled automated quantification of microstructural features. This study proposes two image-based contact angle-measurement approaches: the “liquid-pixel” and “regression” approaches. The study also investigates “center” identification for contact angle measurement. Statistical evaluation of the measurements is performed for both methods and the observed results are discussed. It is concluded that the “non-zero-intercept” approach, one variation within the regression-based techniques, gave the most reliable angle measurement.

Citation information: please cite this work as follows

Motalleb Nejad, M., Manahiloh, K.N., and Meehan, C.L., *Applying the Techniques of Microstructural Image Processing Toward Measuring Interface Angles in Unsaturated Geomaterials*, in *Geotechnical Frontiers 2017: Geotechnical materials, modeling, and testing*, GSP 280.

Link to published article: <https://ascelibrary.org/doi/abs/10.1061/9780784480472.070>

INTRODUCTION

The advent of microstructural imaging technologies such as industrial X-ray micro-CT and bench top synchrotron X-ray CT has facilitated the development of soil mechanics research at the pore-scale. Microstructural examination of multi-phase media has benefited, in particular, from such advancements (Andrew et al. 2014; Manahiloh and Meehan 2015, 2016; Manahiloh and Muhunthan 2012; Wildenschild and Sheppard 2012).

Hydraulic conductivity and suction have a dominant influence on multiphase flow in partially saturated media (Andrew et al. 2014). These macroscale parameters are in turn controlled by pore-scale topology, interfacial tension, and contact angle (Andrew et al. 2014). Contact angle has been defined as the angle measured from the liquid-solid interface to the liquid-air interface (Jury and Horton 2004), and it is believed to be an intrinsic property of any two contacting phases in a solid-liquid-air system (Lu and Likos 2004). Following Jury and Horton's (2004) definition of contact angle and accounting for solid particle and liquid phase curvature for unsaturated soil systems, the contact angle can be defined as the angle between a lines tangent to the solid-liquid and a liquid-air interfaces. Generally speaking, contact angle is a widely used measure of the wettability of surfaces (Anderson 1986).

A review of available literature reveals a number of contact angle measurement techniques. Some commonly utilized approaches include the dynamic sessile drop method (Dickson et al. 2006; Espinoza and Santamarina 2010), the captive bubble method (Chiquet et al. 2007), and methods that use micro-model studies (Chalbaud et al. 2009). Manahiloh and Meehan (2015, 2016) highlighted that the utility of such measurement methods is limited to cases where the solid is a flat plate. For the majority of geomaterials that come in contact with water, nonlinear interfacial surfaces dominate the solid-liquid interactions. In an attempt to develop a contact angle measurement method that could work for curved interfaces, Manahiloh and Meehan (2015, 2016) used an image-based angle measurement approach and demonstrated this direct technique on a X-ray micro-CT images of an unsaturated granular specimen comprised of spherical glass beads. In their work, the contact angle quantification was not automatic. Instead, a series of user-influenced image post-processing algorithms were employed to draw tangent lines for the solid-liquid and liquid-air interfaces and to measure the angles in between.

In this work two angle measurement approaches are developed and used to compute interphase contact angle from images of an unsaturated granular media. The advantages and disadvantages of each method are discussed and practical recommendations, for the most appropriate use of the methods, are made.

MATERIALS AND METHODS

Materials. A three-phase microstructural image of an idealized unsaturated granular media is segmented into pixels containing three gray-values, as shown in Figure 1 and used for analysis. The unsaturated granular media is assumed to idealize a random mixture of granular solid particles, liquid, and gas phases. Image segmentation is one of the key steps in image processing. It uses predefined algorithms to cluster gray values of pixels into finite number of classes. In the three-phase segmented image shown in Figure 1, the dark black, gray, and white pixels represent the solid, liquid, and gas phases of the idealized unsaturated granular media, respectively.

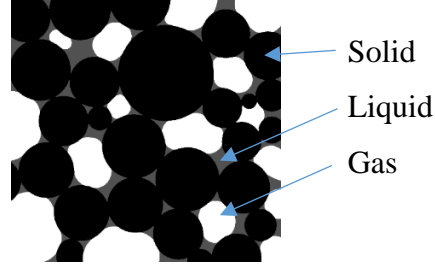


Figure 1. Segmented image of an idealized unsaturated granular medium.

Establishing the “Center” for Contact Angle Measurements. The first step in estimating the interfacial contact angles is to identify a “center” for each contact point. The term “center”, in this study, refers to the coordinates of the points where three phases meet in a given segmented image. A given two-dimensional (2D) image (e.g., Figure 1) may contain multiple center points, distributed over the area of the image. In order to estimate the coordinates of all the centers, algorithms that follow certain criteria need to be established. One simple way to identify a center is to define a two-by-two pixel “window” (W) and evaluate the gray values of all pixels (P) of the image as the window scans the entire image. For example, for a pixel located on row i and column j of the image matrix, this window (W) can be written as:

$$W = \begin{bmatrix} P_{(i,j)} & P_{(i,j+1)} \\ P_{(i+1,j)} & P_{(i+1,j+1)} \end{bmatrix} \quad (1)$$

As the “window” moves throughout the image, if the frequency of the gray values read at all phases are found to be equal or greater than one, the center coordinates of such a window will be taken as the location of one “center” in the image.

In order to find the “centers” in an image, one needs to use two numbering systems (one counting pixels in the image and the other counting the number of corners) and a defined coordinate system. Figure 2 shows the respective pixel and corner numbers, and the coordinates of each for a three-by-three image matrix. In the figure, pixels and corners are indicated by the letters P and E , respectively. Figure 2 also shows that, for m rows and n columns of pixels, there are $m-1$ rows and $n-1$ columns of corners and each corner is surrounded by 4 pixels. Following our simplistic definition of a “center” as *the corner at which three different gray-valued pixels meet*, in Figure 2, the corner $E_{(2,2)}$ with coordinates: $[x, y] = [2.5, 2.5]$ qualifies for a center. The simplest way of finding this corner is to evaluate all two-by-two matrices (i.e., “windows”) and find the matrices for which the frequency for all phases are equal to or greater than one. It should be noted that in Figure 2, $E_{(2,2)}$ is the estimated location of a center, and the exactness of it being the real center is restricted by the quality of the image. In this regard, low-resolution images could lead to identification of erroneous centers. The higher the resolution of the image, the higher the accuracy of the center identification process that is performed.

In order to reduce computational time, the image processing algorithm could be instructed to not evaluate submatrices for windows that could be written as $W = \lambda_n I$, with λ being one of the pixel values assigned to each phase and I being a two-by-two identity matrix.

Any disturbance (noise) resulting from image segmentation could be another source of error in center determination. Depending on the technique that is adopted for image segmentation, some degree of disturbance is introduced near the boundaries close to the phase-separation thresholds. Such an error becomes more pronounced at corners where the three-phases meet (i.e., the centers). Such a point is shown in Figure 3 (look at the central square with a corner point shown

with a dot). The profile of the solid-liquid boundary gets noisy upon segmentation, especially near the three-phase junction point (i.e., the center).

Another source of error in finding the center is the possibility of finding more than one center point for a single contact angle. Figure 4 shows two cases in which the algorithm detects more than one center point. Such a problem could be solved in two ways. In the first method, a single center can be obtained by averaging the coordinates of the multiple centers obtained for immediate-neighbor windows. The advantage of this method is that it is quick. In the second method, the last liquid pixel that is attached to the solid phase is the target pixel. Once the centers that pertain to a single contact point are detected, the histogram of an n -by- n submatrix will be identified for each of the centers. Then the corner surrounded by pixels with the least liquid-phase-frequency is selected as the correct center. The value of the integer n depends on the rate of disturbance in the window near the center. For example: in Figure 4(a), $n = 2$ and in Figure 4(b), $n = 4$ to enable detection of the proper center.

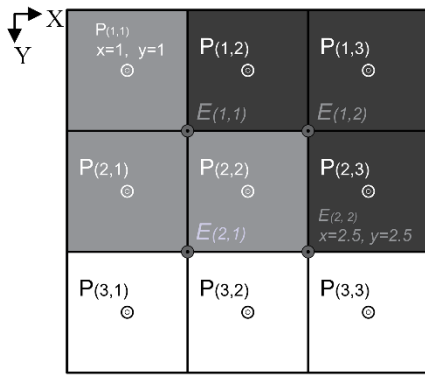


Figure 2. Numbering systems and coordinate system for a schematic image.

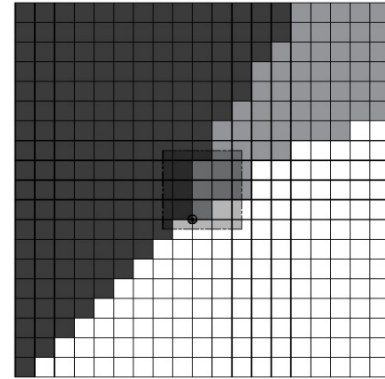


Figure 3. Noise (disturbance) during segmentation.

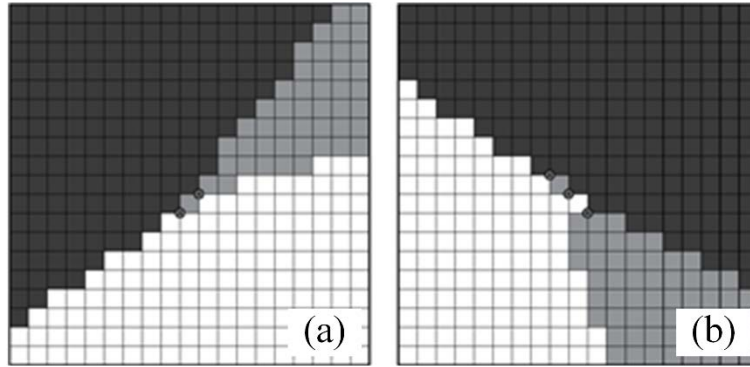


Figure 4. Multiple centers found for a single contact angle.

CONTACT ANGLE MEASUREMENT METHODS

“Liquid-Pixel” Approach (Method 1): Having determined the center points for contact angle measurement, one needs to develop an automated method to estimate contact angle. One simple method is to count the liquid pixels (LP) that are located at a radial distance r from the center point. This method, however, becomes ineffective for small values of r . For example, for $r = 1$, the

contact angle will always be estimated as $\pi/2$. In order to avoid such an error, the radial distance at which the liquid pixel counting is done needs to be larger.

The coordinates of a point on the circumference of a circle, with radius r and center coordinates (X_c, Y_c) , can be defined by the following expressions:

$$\left. \begin{aligned} X &= r \times \cos(\alpha) + X_c \\ Y &= r \times \sin(\alpha) + Y_c \end{aligned} \right\} \quad (2)$$

where, α is the angle subtended by a line that connects the “center” to a “scanning” point and a horizontal line. X_c and Y_c can be estimated by one of the two methods described in the previous section. The “scanning” point is a point on a circle of radius r , on which pixel values are evaluated as the image processing algorithm “scans” each pixel and evaluates its gray-value. The pixel value for the scanning points located on the circle is obtained for increments of $\Delta\alpha_{(\text{degrees})} = 360 / N_\alpha$. Here, N_α represents the number of scanned points on the circumference of the circle and its value controls the accuracy of the angle measurements. For $N_\alpha = 360$, the image processing algorithm scans points at a one degree interval. The higher the value of N_α , the more scanning points that are utilized and the higher the accuracy of the angle measurement. In this study, a value of $N_\alpha = 10,000$ was utilized, which means that 10,000 points are scanned over the circumference of the circle of interest. Once all scanning is done for the points of interest, the algorithm counts the number of points with liquid gray values (N_{LP}). The value of the contact angle (θ) is then estimated using the following expression:

$$\theta_{(\text{rad})} = \frac{N_{LP} \times 2\pi}{N_\alpha} \quad (3)$$

For a circle with $r = 5$, Figure 5 shows the above procedure while scanning is proceeding (5a) and after the scanning is completed (5b). For the image shown in Figure 5, the procedure discussed above yields a contact angle value of $\theta_{(\text{rad})} = (1191 \times 2\pi) / 10000 = 0.2382 \pi$, which is equivalent to 42.88° . This approach may not be effective when there is a lack of a smooth transition between pixel boundaries, such as when r is very small. As an example, Figure 6 compares the contact angle values computed for $r = 4.5$, $r = 5.5$, and the average of contact angles calculated for 20 concentric circles with radii between 5 and 10, which yield measured contact angles of 37.26° , 44.06° , and 39.65° , respectively.

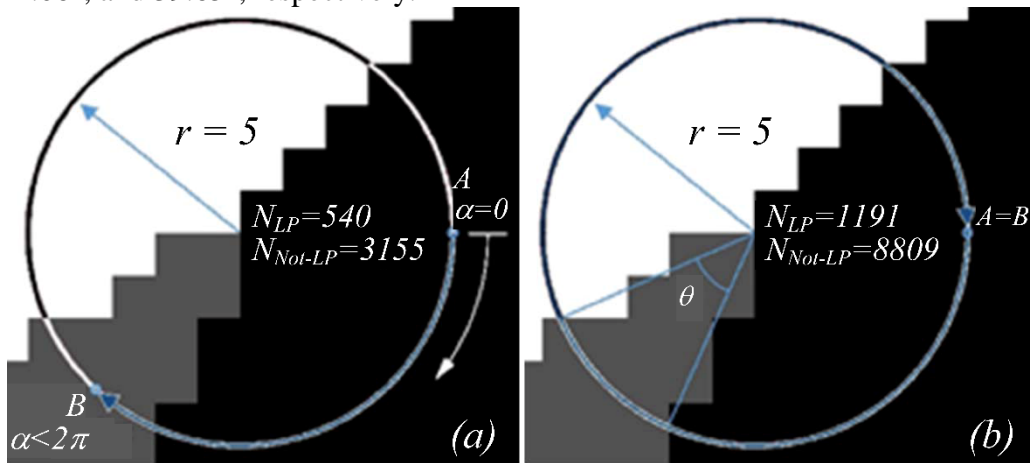


Figure 5. “Scanning”: (a) In progress, and (b) Completed.

It is evident, from the angle measurements shown in Figure 6, that the contact angle that is obtained varies as a function of the size of the circles. This contact angle is also dependent on the

location of the center. The location of the center, in turn, was shown to depend on the method of center selection. A separate analysis was performed to check the sensitivity of the obtained contact angle values to changes in center location (Figure 7). This figure shows angle values obtained for different radii and different methods of finding the center. It can be inferred from Figure 7 that the contact angle is sensitive to both the size of the circle and the approach adopted in locating the center. In Figures 7 (a-c), the center was obtained by averaging the coordinates of the two corners where three-phases meet. In Figures 7(d-e), the center was obtained by looking for the corner of the last liquid-pixel. In general, it was observed that the corresponding contact angle measurements decreased when the center was obtained by the “liquid-pixel” approach.

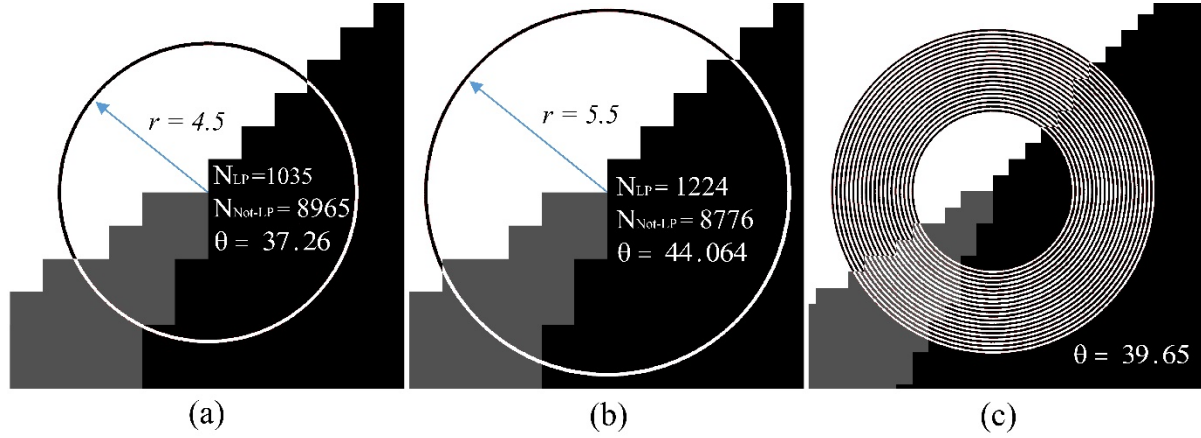
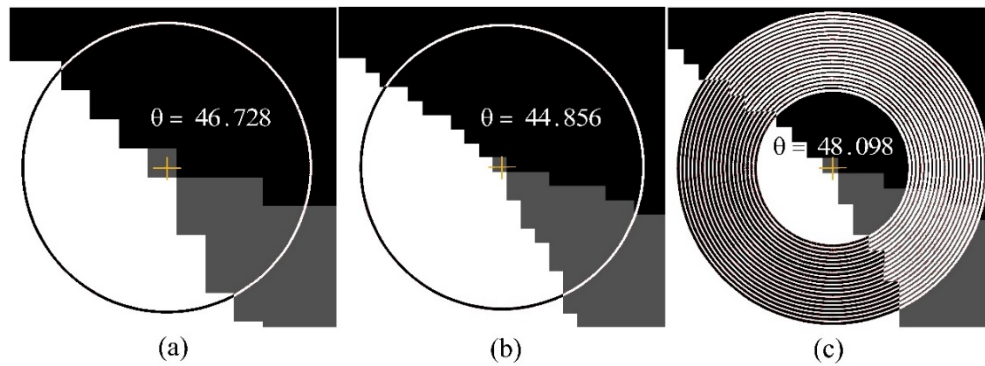


Figure 6. Measuring contact angle: (a) $r = 4.5$, (b) $r = 5.5$, and (c) $r =$ the average of contact angles calculated for 20 circles with radii between 5 and 10.

To summarize, two important factors influence the values for contact angle. One is the disturbance (noise) introduced to center points during the image segmentation. The second factor was the size (radius) of the circle selected for contact angle evaluation. On one hand, there is a legitimate need for the circle to be close to the center point. On the other hand, the resolution of images may not be high enough to allow the higher values of r (i.e., more pixels fit a given circle when image resolution is high, resulting in large r as compared to the r associated with the same area in low resolution images). For low-resolution images, the pixelation that occurs in the boundaries of the phases, especially at the three-phase corners, prevents the identification of the smooth boundaries for image processing purposes.



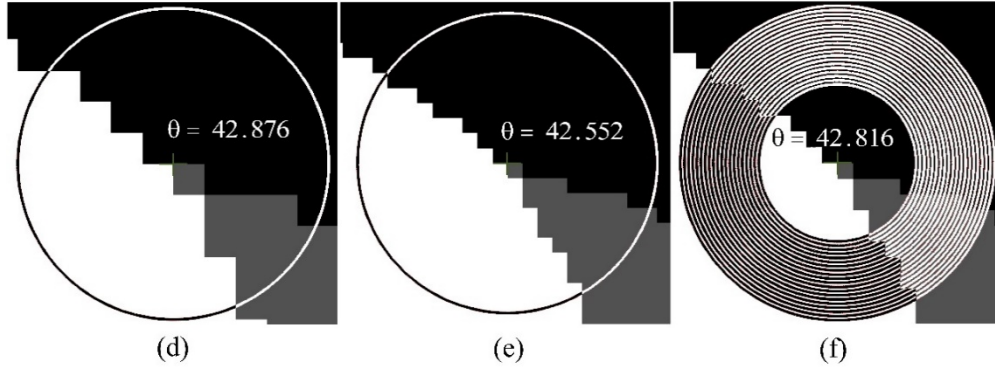


Figure 7. Calculating contact angle: (a and d, $r = 5$), (b and e, $r = 10$), and (c and f, $5 \leq r \leq 10$).

“Regression” Approach (Method 2): Low-resolution images necessitate algorithmic definition of smooth phase boundaries in areas that are close to the “center”. In order to do this, two separate linear regressions could be performed, one for a set of points located at the liquid-gas boundary, and another for a set of points located at the solid-liquid boundary.

The areas of interest (AOI) on which contact angles are measured are very small compared to the dimension (size) of the whole image. This vast size difference might result in a false fit in the linear regression that refers to a global coordinate system (Figure 8). Therefore, it becomes necessary to define a local coordinate system for each identified center point. The local coordinates for the n^{th} point on the phase transition boundary can be obtained by subtracting the global coordinates of the center from the global coordinates of each point. Figure 8 conceptually illustrates the idea of global and local coordinates (obtained with Equation 4).

$$\left. \begin{aligned} x_n &= X_n - X_c \\ y_n &= Y_n - Y_c \end{aligned} \right\} \quad (4)$$

The coordinates of the points used for linear regression can be obtained by looking at circles with different radii. The locus of the points located on the circumference of the circles with different radii are scanned with small angular increments using Equation 3. Two different linear regression methods can then be applied to find the equation of the smooth line tangent to the boundaries of phases at a given contact point.

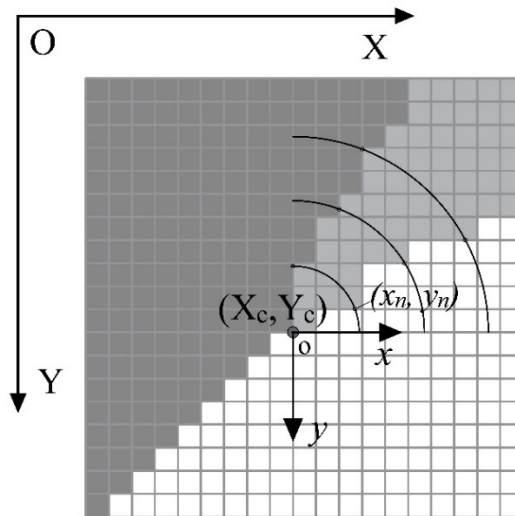


Figure 8. Conceptual illustration of the global and local coordinates.

Zero-Intercept Approach. The first regression approach is based on the assumption that the center point is precisely identified and the disturbance due to image segmentation is negligible. Under such circumstances, the best-fit line should pass through the center point. Therefore, the linear regression is performed with a zero-intercept assumption (Note: This method is referred to here as the “zero-intercept” approach). Then, with the zero-intercept assumed, two regression lines will be fit to the points making up the solid-liquid and liquid-air boundaries. The equations of these fitting lines take the following forms, respectively.

$$Y_{S-L} = mX_{S-L} \quad (5)$$

$$Y_{G-L} = nX_{G-L} \quad (6)$$

Non-Zero-Intercept Approach. The second regression approach accounts for the image being low-resolution and for the introduction of considerable “center” noise during image segmentation. In this case, the estimated coordinates of the center will be used as a reference to the coordinates of the regression points (i.e., they will serve as the origin of the local coordinate system) and won’t be considered as a regression point. In this approach, the fit is not forced to pass through the origin (in this case the center) and the associated regression may result in lines that have a slope and a non-zero y-intercept. The equations for the two lines (i.e., the solid-liquid and liquid-air interface lines), can be written as shown in Equations (7) and (8).

$$Y_{S-L} = mX_{S-L} + Y_{0(S-L)} \quad (7)$$

$$Y_{G-L} = nX_{G-L} + Y_{0(G-L)} \quad (8)$$

Even though there are non-zero intercepts here, the intercepts don’t take a role in obtaining the angle formed between two lines. In order to find the angle between two lines, the only required parameters are the slopes of the lines. Therefore, for both approaches, the angle formed by the intersection of the two lines (i.e., the contact angle) can be calculated as:

$$\theta = \arctan \left| \frac{m - n}{1 + m \times n} \right| \quad (9)$$

In order to examine whether any disturbance has occurred for the contact point or not, one can compare the coefficient of determination (R^2) for both the “zero-intercept” and “non-zero-intercept” approaches. Figure 9 compares the contact angle values obtained for two different center points using the two regression approaches. The results are interpreted by examining their respective coefficients of determination. Nine circles with different radii from 2 to 10 have been used to obtain the regression data.

The results show that the value of R^2 is higher for the “non-zero-intercept” approach. This implies that the center needs to be eliminated from the linear regression. The relatively lower R^2 values obtained for the “zero-intercept” approach show that the disturbance to the center point due to image segmentation is significant and affects the contact angle results. Similar observations were made when the two alternative approaches were applied to other contact angle measurements. Table 1 summarizes five angle measurements that were performed on digital images using the “liquid-pixel” and “the regression-based” approaches. For the “liquid-pixel” approach, measurement of angles was made by considering $r = 5, 10$, and the average of angles measured on

20 equally spaced circles with radii between 5 and 10. For the “regression-based” approach, the “zero-intercept” and the “non-zero-intercept” approaches were employed.

The results in Table 1 show that when r values are small, the effect of pixelation increases the error in measured results using the “liquid-pixel” method. Therefore, in such instances, this method could become unreliable. The values of the contact angle for a “liquid-pixel” approach with $r = 10$ and the “regression-based” approach with “zero-intercept” are very close to each other. However, the coefficient of determination for “zero-intercept” regression is lower than that of “non-zero-intercept”. Therefore, the “non-zero-intercept” regression seems to be the most reliable option for contact angle calculation. The lower angle values obtained in the “non-zero-intercept” regression approach indicate that the contact angles were measured near the center and the effect of disturbance near the center, which is caused by image segmentation, has been eliminated.

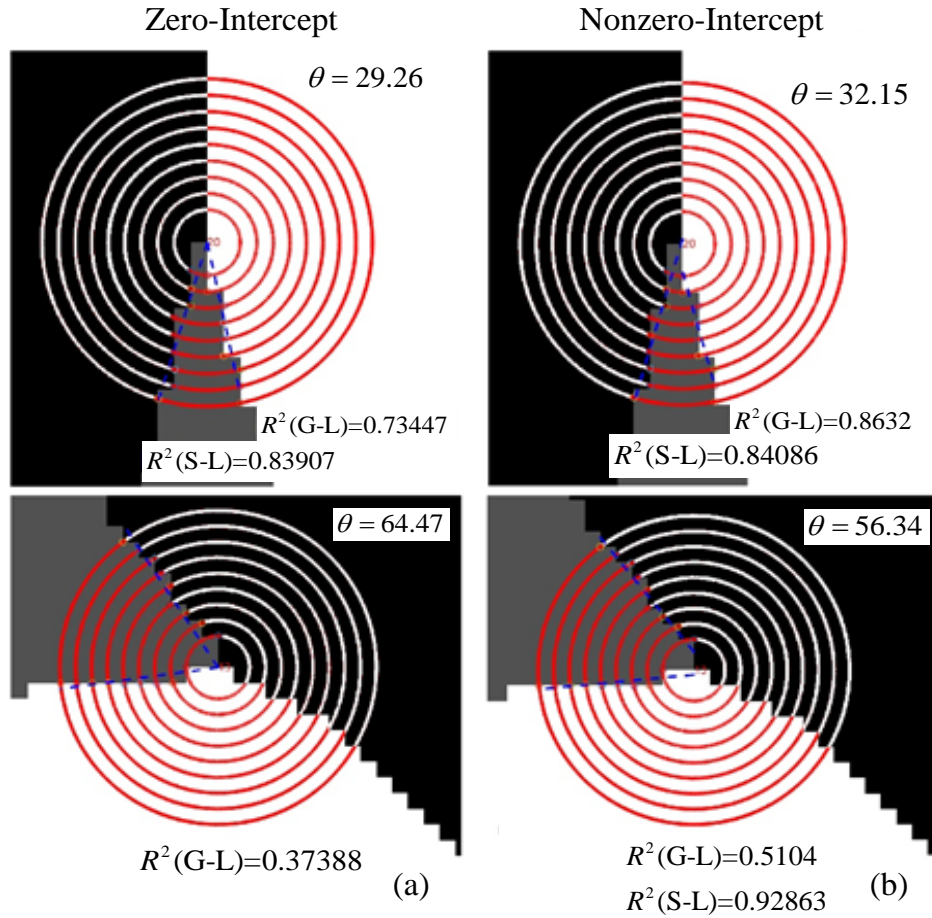


Figure 9. Regression-based contact angle measurements for two different center points: (a) “zero-intercept” approach, and (b) “non-zero-intercept” approach.

Table 1. Comparison between Different Approaches

| No. | “Liquid-Pixel-Based” Approach | | | “Regression-Based” Approach | |
|-----|-------------------------------|----------|--|-----------------------------|-------------------|
| | $r = 5$ | $r = 10$ | Average θ for 20 circles ($5 < r < 10$) | Zero Intercept | Nonzero Intercept |
| 1 | 41.58 | 35.67 | 35.9 | 36.6 | 30.6 |
| 2 | 64.65 | 58.86 | 62.6 | 61.7 | 57 |
| 3 | 29.55 | 36.43 | 37.9 | 37.9 | 33.4 |
| 4 | 53.14 | 47.37 | 46 | 46.7 | 39.5 |
| 5 | 77.97 | 60.01 | 63.4 | 63.8 | 52.2 |

CONCLUSIONS

Two novel methods of contact angle measurement were proposed. The first method, which is called a “liquid-pixel” approach, counts the liquid pixels that lie on a scanning circle of radius r and uses these values to calculate the contact angle. It was highlighted that such a technique depends on the ease of finding the center and the radial distance where liquid pixels were counted. Further, it was discussed that the center is prone to image noise, which is common for images that have been subjected to segmentation. Two regression-based angle quantification methods were introduced. It was shown, with statistical evidence, that the “non-zero-intercept” approach is superior to the “liquid-pixel” and “zero-intercept” regression approaches.

REFERENCES

- Anderson, W. G. (1986). "Wettability Literature Survey- Part 2: Wettability Measurement." *Journal of Petroleum Technology*, 38(11), 1246-1262.
- Andrew, M., Bijeljic, B., and Blunt, M. J. (2014). "Pore-scale contact angle measurements at reservoir conditions using X-ray microtomography." *Advances in Water Resources*, 68, 24-31.
- Chalbaud, C., Robin, M., Lombard, J. M., Martin, F., Egermann, P., and Bertin, H. (2009). "Interfacial tension measurements and wettability evaluation for geological CO₂ storage." *Advances in Water Resources*, 32(1), 98-109.
- Chiquet, P., Broseta, D., and Thibeau, S. (2007). "Wettability alteration of caprock minerals by carbon dioxide." *Geofluids*, 7(2), 112-122.
- Dickson, J. L., Gupta, G., Horozov, T. S., Binks, B. P., and Johnston, K. P. (2006). "Wetting phenomena at the CO₂/water/glass interface." *Langmuir*, 22(5), 2161-2170.
- Espinoza, D. N., and Santamarina, J. C. (2010). "Water-CO₂-mineral systems: Interfacial tension, contact angle, and diffusion—Implications to CO₂ geological storage." *Water Resources Research*, 46(7), W07537.
- Jury, W. A., and Horton, R. (2004). *Soil Physics, Sixth Edition*, Wiley, Hoboken, New Jersey.
- Lu, N., and Likos, W. J. (2004). *Unsaturated Soil Mechanics*, Wiley, Hoboken, New Jersey.
- Manahiloh, K. N., and Meehan, C. L. (2015). "Evolution of interphase contact angle in partially saturated soils using digital analysis of X-ray computed tomography images." *Geotechnical Special Publication*(256), 2092-2101.
- Manahiloh, K. N., and Meehan, C. L. (2016). "Determining the Soil Water Characteristic Curve and interfacial contact angle from microstructural analysis of X-ray CT images." *ASCE Journal of Geotechnical and Geoenvironmental Engineering*, Under Review.

- Manahiloh, K. N., and Muhunthan, B. (2012). "Characterizing Liquid Phase Fabric of Unsaturated Specimens from X-Ray Computed Tomography Images." *Unsaturated Soils: Research and Applications*, C. Mancuso, C. Jommi, and F. D'Onza, eds., Springer Berlin Heidelberg, 71-80.
- Wildenschild, D., and Sheppard, A. P. (2012). "X-ray imaging and analysis techniques for quantifying pore-scale structure and processes in subsurface porous medium systems." *Advances in Water Resources*, 51, 217-246.